

RSC Advances



This is an *Accepted Manuscript*, which has been through the Royal Society of Chemistry peer review process and has been accepted for publication.

Accepted Manuscripts are published online shortly after acceptance, before technical editing, formatting and proof reading. Using this free service, authors can make their results available to the community, in citable form, before we publish the edited article. This *Accepted Manuscript* will be replaced by the edited, formatted and paginated article as soon as this is available.

You can find more information about *Accepted Manuscripts* in the [Information for Authors](#).

Please note that technical editing may introduce minor changes to the text and/or graphics, which may alter content. The journal's standard [Terms & Conditions](#) and the [Ethical guidelines](#) still apply. In no event shall the Royal Society of Chemistry be held responsible for any errors or omissions in this *Accepted Manuscript* or any consequences arising from the use of any information it contains.



ARTICLE

High capacity MnFe₂O₄/rGO nanocomposite for Li and Na-ion battery applications[†]

Pratap Kollu^{*a}, P. Ramesh Kumar^b, Chella Santosh^c, Do Kyung Kim^{*b} and Andrews Nirmala Grace^{*c}

Received 00th January 20xx,
Accepted 00th January 20xx

DOI: 10.1039/x0xx00000x

www.rsc.org/

Porous MnFe₂O₄/reduce graphene oxide (rGO) nanocomposite with high storage capacity was prepared by a hydrothermal method. MnFe₂O₄/rGO nanocomposite sample was characterized by X-ray diffraction, Raman spectroscopy, scanning electron microscopy and high resolution transmission electron microscopy. The electrochemical characteristics with lithium as well as sodium were found by using cyclic voltammetry and battery cycle tester. In this work, apart from the lithium storage, the sodium storage ability of the spinel type MnFe₂O₄ as an anode is demonstrating for the first time. The prepared MnFe₂O₄/rGO composite with sodium alginate binder shows a high stable capacity of 905 mAh g⁻¹ versus Li/Li⁺ and 258 mAh g⁻¹ versus Na/Na⁺ at 0.1C rate. The enhancement in capacity and excellent cycleability nature in the MnFe₂O₄/reduce graphene oxide nanocomposite is due to constrains of volume expansion during conversion reaction and enhancement of electrical conductivity. Abstract text goes here.

1. Introduction

In recent days, there is an incredible increase for the lithium ion batteries due to their practical applications in electronic devices, hybrid electric vehicles and all types of electric vehicles [1-5]. In order to find an alternative to lithium energy storage systems, researchers have focused on sodium ion batteries. Sodium is very cheap and abundant in earth crust, which makes it the most advantageous element for battery applications after lithium. Furthermore, the interaction chemistry is mostly same like lithium. Present days, most common anode material used in the secondary ion batteries are carbon materials. The drawback of using carbon material as anode leads to lower reversible storage capacity which cannot meet the growing demands of high storage capacity of secondary batteries [6]. It has thus become an imperative to develop an electrode material with low cost, long life, high storage capacity and safety [7-9]. One of the promising materials having high performance as anode materials for secondary ion batteries is transition metal oxides (TMO). The TMO based materials has high capacity as compared with the commercially used graphite material (e.g., 1007 mAh g⁻¹ of Fe₂O₃; 890 mAh g⁻¹ of Co₃O₄; 755 mAh g⁻¹ of MnO; 717 mAh g⁻¹

for NiO) [10, 11]. Also, binary metal oxides also called as spinel ferrites with the general formula MFe₂O₄ (M=Mn, Co, Ni, Zn or Mg) are very fascinating materials due to their interesting electrical and magnetic properties with high thermal and chemical stabilities [12]. Manganese ferrite (MnFe₂O₄) one of the ferrite families is grown as various morphologies such as nanocrystals [13], nanocubes [14] and hollow spheres [15]. Manganese ferrite stores through the conversion reaction mechanism (MnFe₂O₄ + 8X⁺ + 8e⁻ - Mn + 2Fe + 4X₂O; X= Li & Na) and it has high theoretical capacity of 928 mAh g⁻¹, which is much higher than carbon anode (375 mAh g⁻¹). The TMO materials show poor electrochemical performances due to low electronic conductivity. To overcome this problem, doping of high electronic conducting carbon forms to achieve enhanced electrochemical properties is essential.

Besides, graphene based nanocomposites as anodes for rechargeable lithium ion batteries have been extensively investigated, such as graphene - metal composite [16], graphene - metal oxides [17] and graphene - sulfur composites [18]. The decoration of nanoparticles into the graphene sheets will generate a porous network, providing an outstanding electron-conducting and ion-transporting pathway [19, 20]. The theoretical capacity of graphene is 744 mAh g⁻¹, which is twice than that of graphite materials. In case of sodium ion battery, Fe₂O₃/graphene sheet composites [21], and MoS₂/carbon nanofibers [22]...etc, were used as anode materials [23]. Thus, graphene based nanocomposite materials will have enhanced electrochemical performances, particularly charging /discharging process and rate capabilities. In present work, manganese ferrite incorporated in graphene sheets was prepared via solvothermal process. The prepared materials

^aThin Film Magnetism group, Cavendish Laboratory, Department of Physics, University of Cambridge, Cambridge CB3 0HE, United Kingdom, Email: pratapk@iitb.ac.in.

^bDepartment of Materials Science and Engineering, Korea Advanced Institute of Science and Technology (KAIST), Daejeon 305-701, Republic of Korea, Email: dkkim@kaist.ac.kr; Fax: +82-42-350-3310; Tel: +82-42-350-4118

^cCentre for Nanotechnology Research, VIT University, Vellore- 632014, India, Email: anirmalagrace@vit.ac.in

[†] Footnotes relating to the title and/or authors should appear here.

Electronic Supplementary Information (ESI) available: [TGA, CV and cyclic stability for pure MnFe₂O₄]. See DOI: 10.1039/x0xx00000x

were characterized using XRD, Raman, SEM and TEM techniques. The composite was further tested as anode for lithium as well as sodium ion battery applications and results showed that it exhibited high storage capacity and excellent cyclic stability.

2. Experimental

2.1 Synthesis of $\text{MnFe}_2\text{O}_4/\text{rGO}$ composite

Graphene oxide is primary precursor to synthesis the reduced graphene oxide and manganese ferrite nanocomposite ($\text{MnFe}_2\text{O}_4/\text{rGO}$), which was prepared from natural graphite by a modified Hummer's method [24]. Manganese ferrite nanocomposite was synthesized from our previous work [25]. In a typical procedure, 300 mg of graphene oxide, 3 mmol of manganese chloride ($\text{MnCl}_2 \cdot 4\text{H}_2\text{O}$) and 6 mmol of ferric chloride ($\text{FeCl}_3 \cdot 6\text{H}_2\text{O}$) were mixed and dissolved in an appropriate amount of ethylene glycol followed by ultrasonication for more than 2 h. Then the mixture was subjected to stirring by adding sodium acetate and polyethylene glycol about for a certain time. The product was sealed in Teflon coated hydrothermal bomb and kept in hot-air oven at 200°C for 10 h. Finally, after reaching to room temperature, the product was separated by centrifugation for several times in water and ethanol followed by drying at 60°C .

2.2 Characterization

x-ray diffraction patterns (XRD) were recorded on a Rigaku Miniflex using the $\text{Cu K}\alpha$ radiation ($\lambda = 1.5406 \text{ \AA}$) over 2θ range from 10° – 80° . The microscopic feature of the samples was characterized by field-emission scanning electron microscopy (SEM) Hitachi S-4800 and high-resolution transmission electron microscopy (HR-TEM) with Energy Dispersive Spectrometer (EDS) (JEOL- 2000EX, JEOL, Tokyo, Japan) operated at 120 kV. Raman measurements were carried out in the back

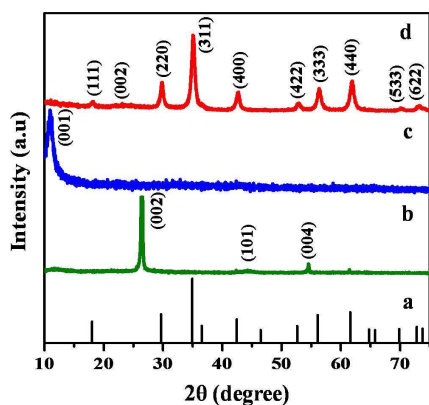


Figure 1: X-ray diffraction pattern of (a) MnFe_2O_4 JCPDS data, (b) Graphite, (c) Graphene oxide and (d) $\text{MnFe}_2\text{O}_4/\text{rGO}$ nanocomposite.

scattered geometry using an (He–Ne laser) laser excitation source emitting at 514 nm with 20 mW power coupled with an ARAMIS (Horiba Jobin Yvon, France) micro-Raman spectrometer. Elemental analysis (EA) experiment was carried out by using Thermo Scientific Flash 2000 Series element analyser. Thermogravimetric (TG) analysis was carried out on Q600 (TA Instruments, USA) at a heating rate of 5°C min^{-1} in air (200 ml min^{-1}).

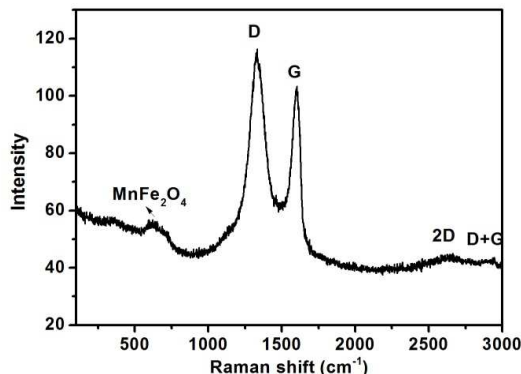


Figure 2: Raman spectra of as-prepared material $\text{MnFe}_2\text{O}_4/\text{rGO}$

2.3 Electrochemical measurement

Electrochemical studies of the synthesized $\text{MnFe}_2\text{O}_4/\text{rGO}$ nanosphere were carried out in CR2032 type cells. The electrode composite consists of 70% active material, 20% Super P carbon and 10% Na-alginate in DI water solvent. The above mixture was grounded properly to form slurry. The slurry was coated on to a Cu-foil and dried at room temperature overnight. The dried Cu-foil was cut into circular electrode disks. The CR2032 type cells were assembled in Argon filled glove box by using celgard 2400 as separator. Lithium and sodium metals were used as counter electrodes. 1 M LiPF_6 in ethylene carbonate (EC) and diethyl carbonate (DEC) (1:1 v/v %) was used as electrolyte for Lithium ion batteries. In case of sodium, 1M NaClO_4 in propylene carbonate (PC) and fluoroethylene carbonate (FEC) (98:2 v/v%) was used as electrolyte. The galvanostatic charge-discharge studies were carried out at different C-rates in the voltage range of 3 - 0.002 V using a battery cycle tester (Wonatec, Korea).

3. Results and Discussion

3.1. Structural analysis

The XRD diffraction pattern of natural graphite powder, graphene oxide and $\text{MnFe}_2\text{O}_4/\text{rGO}$ along with JCPDS data were shown in Figure 1. From figure 1b, Natural graphite flake shows a lattice planes of (002), (101) and (004) at 26.4° , 42.5° and 54.6° respectively with 3.38 \AA spacing between the layers. As seen from the pattern after oxidation, graphitic peak (002) disappeared and a new peak at 11.08° with a lattice structure of (001) of GO was observed (Fig. 1c), whereas for GO the

spacing between the layers were 8.2 Å with a lattice plane at 11.08° suggesting that natural graphite flakes were converted into rGO. In the XRD pattern of MnFe₂O₄/rGO (Fig. 1d), the disappearance of the peak at 11.08° confirms the detachment of oxygen groups and reduction of graphene oxide to graphene nanosheets. Diffraction peaks at 2θ values of 18.03°, 30.18°, 35.46°, 43.02°, 53.81°, 56.89°, 62.55°, 70.20° and 73.3° were observed which correspond to (111), (220), (311), (400), (422), (333), (440), (533) and (622) crystal planes of MnFe₂O₄ in accordance with the standard JCPDS no. 742403. The peaks were broad indicating the nanocrystalline nature of the material. Under these experimental conditions, no other diffraction peaks were obtained, which indicates that the prepared material is of high purity.

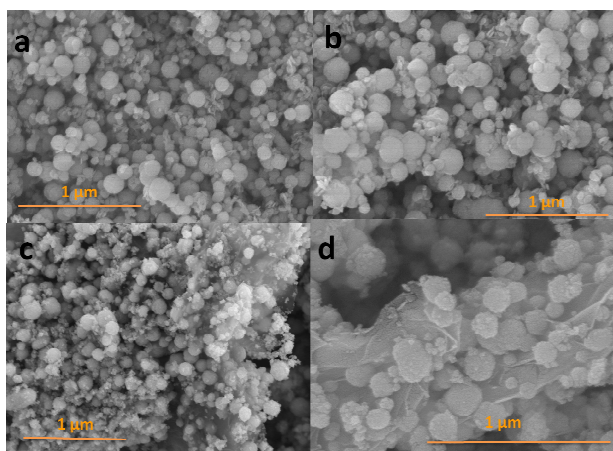


Figure 3: FE-SEM images of a & b) the pure MnFe₂O₄ and c & d) as-prepared material MnFe₂O₄/rGO.

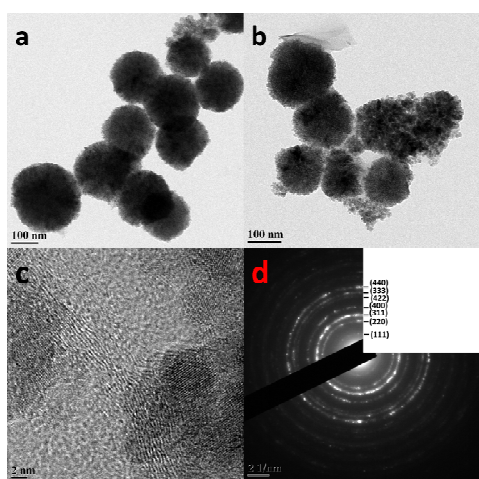


Figure 4: HR-TEM images of MnFe₂O₄/rGO with SADE pattern.

For the reference, Pure MnFe₂O₄ xrd patterns along with JCPDS data was shown in figure S1. Raman spectroscopy is one of the techniques, to know the defects in the sp² carbon

materials. As shown in the Figure 2, the Raman spectra of as-prepared material MnFe₂O₄/rGO have peaks at 1340, 1595, 2680 and 2947 cm⁻¹ are assigned to D, G, 2D and D+G-bands respectively and a weak peak at 615 cm⁻¹ was assigned to the MnFe₂O₄ nanoparticles [26].

3.2. Morphological & Thermo-gravimetric analysis

The surface morphology and particle size of the as-prepared MnFe₂O₄/rGO nanocomposite were further analyzed by FE-SEM and HR-TEM. From the FE-SEM images as shown in Figure 3, it was observed that the MnFe₂O₄ nanoparticles were well decorated as homogeneous spherical particles onto the graphene sheets and the estimated cluster size was ~ 130 nm. Figure 3c and d shows the SEM images of the MnFe₂O₄/rGO nanocomposite in different magnifications. From figure 3d, the MnFe₂O₄ nanoclusters were sandwich between graphene sheets, which is good evidence for the stable electrode operations during the conversion reaction [27]. Structure of the MnFe₂O₄/rGO nanocomposite was further investigated by HR-TEM. HR-TEM images of pure porous MnFe₂O₄ nanostructures at different magnifications are shown in figure 4, which indicated the formation of agglomerated clusters made up off very small nano sized particles with ~120 nm in diameter, which is close that observed from FE-SEM. The SAED patterns were recorded and Debye-Scherrer rings were obtained. These are shown in Figure 4d and represented as (111), (220), (311), (400), (422), (333), (440), (533) and (622) lattice planes, which are supported by the XRD analysis. Furthermore, from elemental analysis, the carbon content in this composite is 19 wt. %. Hence it is confirmed from the above analysis that the solvothermal route offered a homogeneous synthesis of the composite.

Furthermore, thermo-gravimetric analyses of the composite were carried out in air to know the phase changes and decomposition details. MnFe₂O₄/rGO composite was heated to 1000 °C at a rate of 5 °C min⁻¹ and the corresponding TG and DTA curves for MnFe₂O₄/rGO composite is given in fig S2. The TGA measurement identifies the weight loss of the materials from 35 °C to 1000 °C. The weight loss below 100 °C is ascribed to be desorption of physically adsorbed moisture. Furthermore, weight loss above 150 °C is due to decomposition of ethylene glycol, whereas from 500° - 800 °C, a plateau is observed which could be due to the partial decomposition of the sample to form monophasic MnFe₂O₄ [28, 29]. After 750 °C, there is an abrupt decrease in weight (%), which could be due to burning of graphene. This temperature is slightly higher as it is in the form of composite with MnFe₂O₄ [30]. From figure S2, the loading percentage of graphene was calculated from TGA of MnFe₂O₄/rGO. As observed, the decomposition of graphene starts after 750 °C with a corresponding weight loss of 21% (calculated from the difference in weight % in the declination of the weight (%) curve on the left y-axis after 750 °C). Thus taking into consideration the weight loss due to absorbed moisture, EG molecules and graphene, the loading of MnFe₂O₄ is 79%.

3.4.2. Electrochemical analysis

The cyclic voltammetry of $\text{MnFe}_2\text{O}_4/\text{rGO}$ versus Li & Na for twenty cycles between 3 to 0.002 V at a scan rate of 0.2 mV s^{-1} are shown in figure 5a and b respectively. From Fig. 5a, in the first cycle, a large cathodic peak located around 0.5 V vs. Li/Li^+ can be associated with the reduction reactions of Fe^{3+} and Mn^{2+} with Li and the formation of Li_2O during the first discharge process. In the subsequent cathodic scans, $\text{MnFe}_2\text{O}_4/\text{rGO}$ nanoclusters show a cathodic peak and anodic peak at 0.7 V and 1.6 V vs. Li/Li^+ and can be attributed to the reductive reaction of Fe_2O_3 and MnO to Fe and Mn metal, respectively. The $\text{MnFe}_2\text{O}_4/\text{rGO}$ composites show all redox reaction peaks for MnFe_2O_4 nanoparticles. After the first cycle, the intensity of redox peaks remains constant which indicates the electrode stability [31]. From figure S1, the cyclic voltammogram of pure MnFe_2O_4 intensity of peaks changes with cycle numbers, which indicates lower stability against lithium. Figure 5 b shows the CV profile for $\text{MnFe}_2\text{O}_4/\text{rGO}$ composites versus Na/Na^+ . In figure 5b, The observed anodic peaks at 1.6 and 1.85 V correspond to oxidation of Fe^0 to Fe^{3+} and Mn^0 to Mn^{2+} [32]. The broad cathodic peak centered at 0.75 V is attributed to the reduction reactions of Fe^{3+} and Mn^{2+} with Na and the formation of Na_2O during the discharge process.

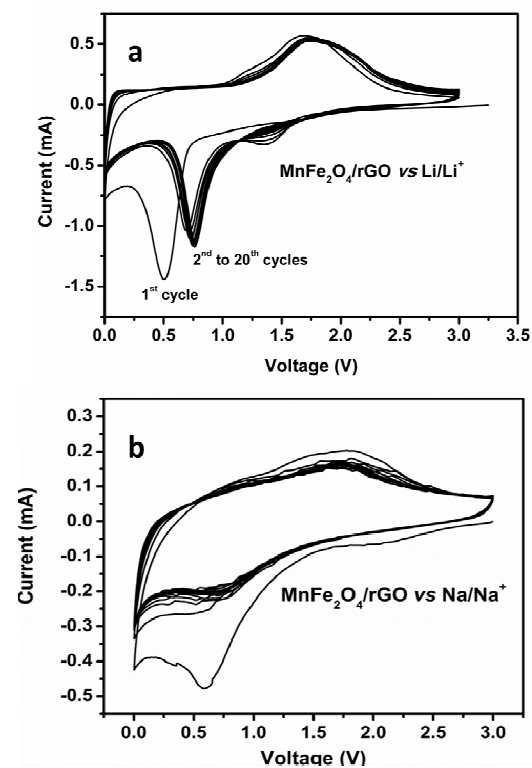


Figure 5: Cyclic voltammetry plots for the a) $\text{MnFe}_2\text{O}_4/\text{rGO}$ vs Li/Li^+ and b) $\text{MnFe}_2\text{O}_4/\text{rGO}$ vs Na/Na^+ composites

The $\text{MnFe}_2\text{O}_4/\text{rGO}$ was showing good rate capability and cycling stability due to the 2D graphene structure which will provide the conductive path for electron transportation and

also it will accommodate the volume expansion while charging/discharging. Furthermore, alginate binder has better adhesive nature with the current collector and anode material during conversion reaction. The alginate binder effect on one of the spinel transition metal oxide has been demonstrated in our previous reports [33]. Hence, the capacity fading is minimized in the lithium ion battery fabricated with $\text{MnFe}_2\text{O}_4/\text{rGO}$ anode and alginate binder. This is reflected in the discharge capacity retention up to few numbers of cycles. Figures S4a and b show the voltage profile and charge/discharge capacity vs. cycle number plots for the pure MnFe_2O_4 electrode at 0.1 C rate. From figure S4a, pure MnFe_2O_4 electrode delivers discharge capacity of 990 mAh g^{-1} at first discharge. The capacity fading is observed when the number of cycle is increasing. A deep fall in the discharge capacity from the initial value to 405 mAh g^{-1} in the 30th cycle is observed. This lower cyclic stability is reflected the previous mentioned CV results. The observed low stable cyclability in pure MnFe_2O_4 electrodes versus Li is might be due to low electronic conductivity and nano sized particles in cluster dissolution in electrolyte while charging-discharging.

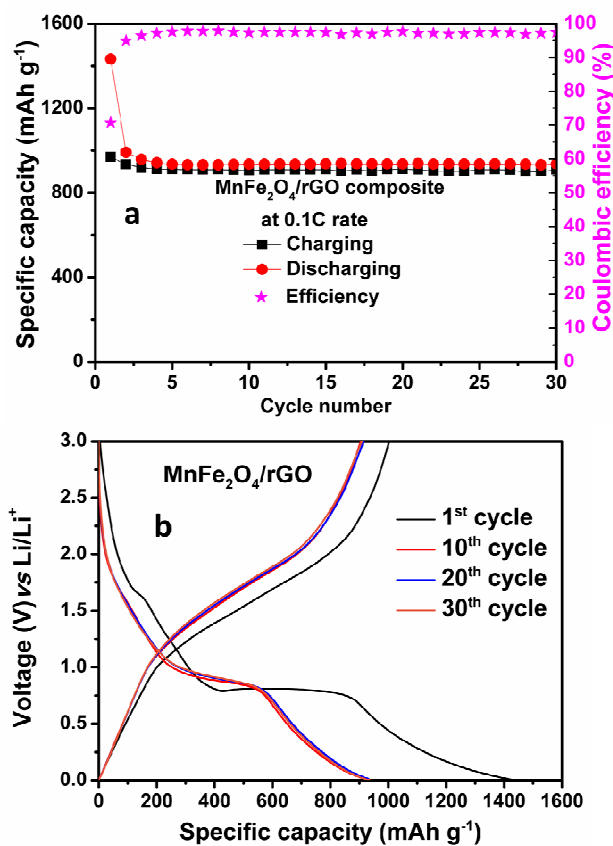


Figure 6: a) cyclic stability and b) charge-discharge curves for the $\text{MnFe}_2\text{O}_4/\text{rGO}$ composites vs Li/Li

The cycleability and charge discharge curves for the $\text{MnFe}_2\text{O}_4/\text{rGO}$ versus Li/Li^+ material are shown in figure 6. From figure 6, the $\text{MnFe}_2\text{O}_4/\text{rGO}$ has delivered stable capacity of 905 mAh g^{-1}

at 0.1C rate for 30 cycles with excellent coulombic efficiency. The $\text{MnFe}_2\text{O}_4/\text{rGO}$ composites presented the extra 1st discharge capacity, is due to the reversible formation and decomposition of polymeric gel-like films on the active particles [34, 35]. The significance of our $\text{MnFe}_2\text{O}_4/\text{rGO}$ composite was its increased capacity at 0.1C and cyclic stability compared to recently reported $\text{Co}_3\text{O}_4@\text{graphene}$ Composites [10], $\text{Fe}_3\text{O}_4/\text{rGO}$, [36] and NiFe_2O_4 nanoparticles [37]. The enhancement of electrochemical properties of $\text{MnFe}_2\text{O}_4/\text{rGO}$ versus Li/Li^+ can be due to the better electronic conductivity network. The discharge profile versus sodium was shown in figure 7. From figure 7a, the $\text{MnFe}_2\text{O}_4/\text{rGO}$ vs Na/Na^+ has delivered stable capacity of 258 mAh g^{-1} at 0.1C rate for 50 cycles. Furthermore, we are the first group who demonstrated $\text{MnFe}_2\text{O}_4/\text{rGO}$ composite as an anode for sodium ion batteries. From figures 6 and 7, two things are clearly observed when the $\text{MnFe}_2\text{O}_4/\text{rGO}$ composite is using as anode for Li and Na-ion batteries. First, the shape difference in charge-discharge curves. The charge-discharge curves of $\text{MnFe}_2\text{O}_4/\text{rGO}$ versus Li/Li^+ has shows one voltage plateau at 0.8 V, but $\text{MnFe}_2\text{O}_4/\text{rGO}$ versus Na/Na^+ charge-discharge curves does not shows any plateau region. Second, capacity difference, $\text{MnFe}_2\text{O}_4/\text{rGO}$ composite has high Li storage capacity than Na capacity. The above mentioned two differences between Li and Na-ion batteries are may be due to the low ionic diffusivity of Na-ion.

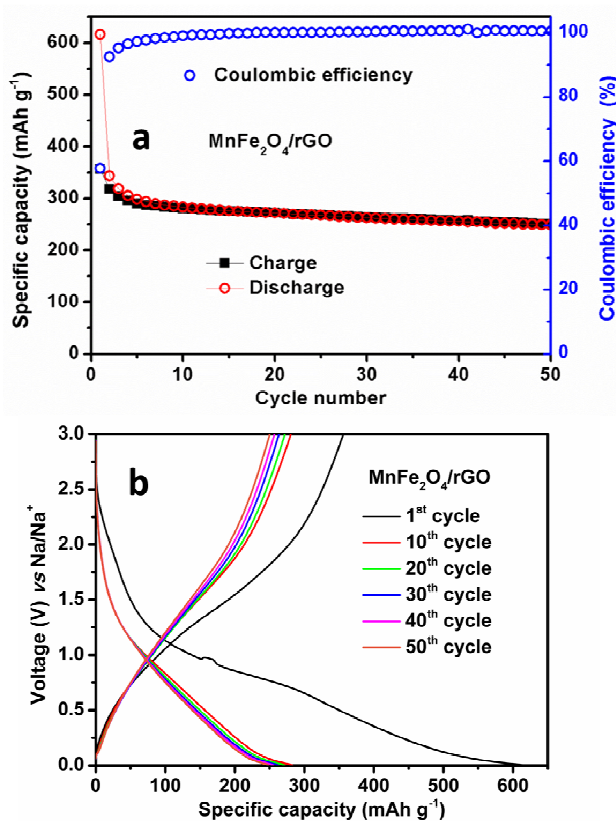


Figure 7: a) cycling stability and b) charge-discharge curves for the $\text{MnFe}_2\text{O}_4/\text{rGO}$ composites vs Na/Na^+

The voltage vs. cycle number and discharge profile for the battery fabricated with $\text{MnFe}_2\text{O}_4/\text{rGO}$ at different current rates are shown in figures 8 a-d respectively. From figures 8a & b, discharge capacity of the anode versus Li/Li^+ decreases to 720, 580, 320, 160 and 60 mAh g^{-1} when current rate increased to 1 C (920 mA g^{-1}), 2 C (1840 mA g^{-1}), 5 C (4600 mA g^{-1}) and 10 C (9200 mA g^{-1}), respectively. From figures 8c & d, discharge capacity of the anode versus Na/Na^+ with different current rates are 98 mAh g^{-1} (920 mA g^{-1}), 58 mAh g^{-1} (1840 mA g^{-1}), 22 mAh g^{-1} (4600 mA g^{-1}) and 8 mAh g^{-1} (9200 mA g^{-1}). The high rate capability and good reversibility are due to the good electronic conductivity, higher surface area and excellent adhesive properties of 2D graphene and alginate binders [38]. The cross linking hydrocarbon chain and swelling nature of alginate binder, maintains good electrical contact between the current collector and anode material upon continuous conversion.

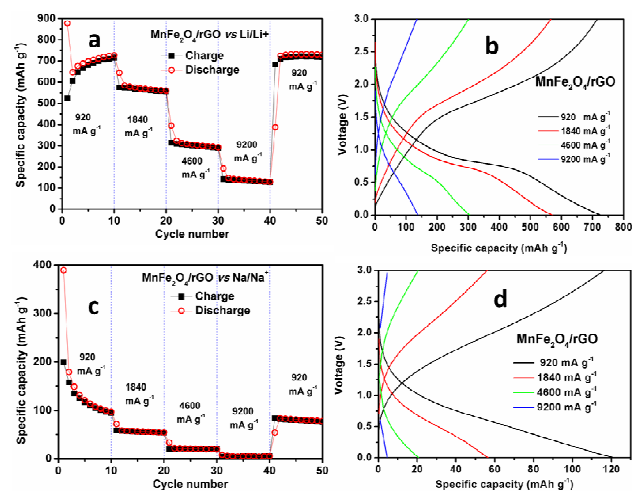


Figure 8: a & c) rate capability and b & d) charge-discharge curves at different rates for the $\text{MnFe}_2\text{O}_4/\text{rGO}$ composites vs Li/Li^+ and Na/Na^+ respectively.

Xuefeng et al., successfully demonstrated reaction mechanism of $\text{MnFe}_2\text{O}_4/\text{Graphene}$ composites versus Li/Li^+ using ex-situ XRD and TEM analysis [32]. Here, first time the path of reaction mechanism of $\text{MnFe}_2\text{O}_4/\text{Graphene}$ composites versus Na/Na^+ during discharging and charging was observed by using ex-situ TEM for the 1st discharge and 1st charge electrodes. Figure 9a & b shows the ex-situ TEM image and SAED patterns for the 1st discharge $\text{MnFe}_2\text{O}_4/\text{rGO}$ composite versus Na/Na^+ . From figures 9 a & b, the retention of morphology and the inter planer distance are derived by measuring the distance between bright rings about the center. The obtained, inter planer distance values are matched to the Miller indices of pure Fe, Mn and Na_2O . The ex-situ TEM results for the fully charged $\text{MnFe}_2\text{O}_4/\text{rGO}$ composite electrode are shown in figure 9 c & d. In figure 9c, the morphology is totally changes from nanoclusters to tiny metal oxide particles which are bounded in graphene network. SAED patterns of fully charged electrode in figure 9 d and it is observed that the formation of Fe_2O_3 and MnO at charge

state. Hence, it is proved that the Fe, Mn metals and sodium oxide formed at discharge state and the formation of Fe_2O_3 and MnO at charge state. Furthermore, we have taken ex-situ XRD for the 1st discharge and 1st charge electrodes, but it is very hard to find corresponding peaks in X-ray diffraction. The XRD patterns for 1st discharge and 1st charge electrodes along with their JCPDS data are shown figure S3. Hence, it is confirmed that formation of Fe_2O_3 and MnO at charged state using ex-situ TEM results, which the direct evidence for conversion reaction mechanism as is proposed in earlier section.

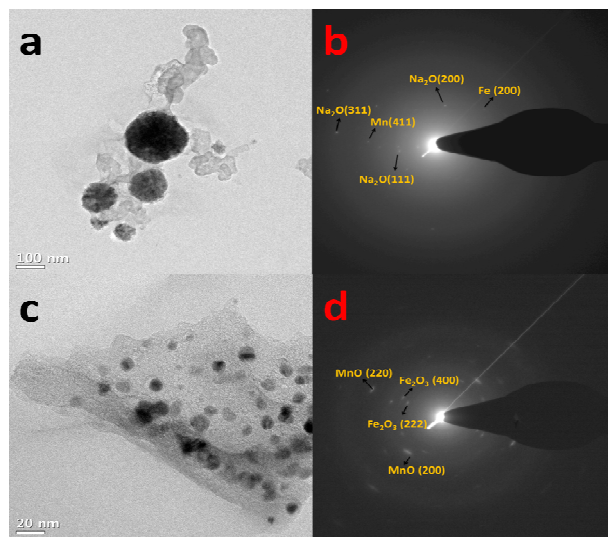


Figure 9: Ex-situ TEM results of $\text{MnFe}_2\text{O}_4/\text{rGO}$ composites vs Na/Na^+ electrodes a, b) images and SAED patterns for 1st discharge state and c, d) image and SAED patterns for 1st charge state.

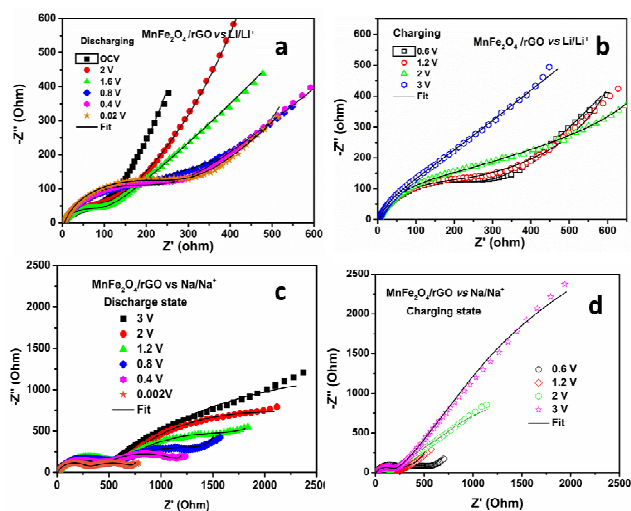


Figure 10: Nyquist plots for the $\text{MnFe}_2\text{O}_4/\text{rGO}$ a & b) vs Li/Li^+ and c & d) vs Na/Na^+ during the charging-discharging.

Figures 10 a–d, show the Nyquist plots for the $\text{MnFe}_2\text{O}_4/\text{rGO}$ composite electrode at discharging and charging states versus Li and Na. In figures 10a & b, we can observe that there is one depressed semicircle with spike in the lower frequency side versus Na. The observed depressed semicircle was fitted by using an $R_{(\text{SF}+\text{CT})}$ combination. From the first dispersed semicircle, $R_{(\text{SF}+\text{CT})}$ resistance values could be estimated from fitted data and presented in table 1. The value of $R_{(\text{SF}+\text{CT})}$ increasing and decreasing during discharging and charging might be due to the solid electrolyte interface (SEI) formation/partial dissolution/re-formation [39]. Figures 10c & d, shows the two distinct semi circles, which are belongs to the RSF and RCT and varying during the charging and discharging states versus Na. From figures 10c and d, it is observed that the values of R at OCV (initial point of discharging state) and 3V (Final point of charging state) are almost equal. Hence, it is confirmed that the SEI between electrolyte and $\text{MnFe}_2\text{O}_4/\text{rGO}$ composite is stable during the discharging and charging. Furthermore, nano-sized porous structures with 2D graphene network offer good charge transfer kinetics due to their high surface to volume ratio.

Table 1: R_e , R_{CT} , R_{SF} , and W_d values of $\text{MnFe}_2\text{O}_4/\text{rGO}$ electrode versus Li and Na during the 1st discharge– charge cycles at various voltages.

Voltage	Li/Li^+			Na/Na^+				
	R_e	$R_{(\text{SF}+\text{CT})}$	W_d	R_e	R_{SF}	R_{CT}	W_d	
Discharging	OCV	80	0.44	4.75	455	3842	0.57	
	2	4.66	102	0.799	5.49	551	2059	0.61
1.2	4.77	87	0.83	6.07	574	1517	0.7	
	0.8	4.84	151	0.85	6.32	1154	461	0.75
0.4	4.86	232	0.83	6.072	385	881	0.77	
	0.02	5.03	243	0.83	5.13	258	621	0.49
Charging	0.6	5.01	251	0.83	5.66	237	342	0.59
	1.2	5.043	218	0.84	5.71	603	185	0.77
2	5.00	210	0.85	5.8	142	3275	0.42	
	3	5.27	141	0.89	6.31	633	184	0.73

4. Conclusions

Spinel manganese ferrite/reduce graphene oxide ($\text{MnFe}_2\text{O}_4/\text{rGO}$) nanocomposite was synthesized from natural graphite by a modified Hummer's method. XRD and Raman results confirmed the formation of $\text{MnFe}_2\text{O}_4/\text{rGO}$ phase and structure respectively. Micro structural analysis was done using SEM and HRTEM, which showed the uniform dispersion of ferrites in graphene sheet network. The $\text{MnFe}_2\text{O}_4/\text{rGO}$ composites delivers a high stable maximum discharge capacity of 905 mAh g^{-1} vs Li/Li^+ and 258 mAh g^{-1} vs Na/Na^+ at 0.1C rate. Here, Na-

alginate binder provided a strong interaction between active material and current collector; further graphene sheets gave the enough void space for the volume expansion during the conversion reaction, act as a barrier to avoid active material dissolution and also it will enhance the electrical conductivity of nanocomposite. Results demonstrated that the $\text{MnFe}_2\text{O}_4/\text{rGO}$ composite material with alginate is a potential anode material for next generation rocking chair battery applications.

Acknowledgements

Authors acknowledge SAIF and Central surface analytical facility of IIT Bombay. Dr. Pratap Kollu acknowledges DST-INSPIRE Faculty award (2012-2017). Prof. D. K. Kim gratefully acknowledges financial support from the Program to Solve Climate Changes (NRF-2010-C1AAA001-2010-0029031) of Korea (NRF) funded by the Ministry of Science, ICT & Future Planning.

References

- P. Poizot, S. Laruelle, S. Grugeon, L. Dupont, J. M. Tarascon, *Nature* 2000, **407**, 496-499.
- Y. J. Lee, H. Yi, W. J. Kim, K. Kang, D. S. Yun, M. S. Strano, G. Ceder and A. M. Belcher, *Science* 2009, **324**, 1051-1055.
- H. L. Wang, L. F. Cui, Y. A. Yang, H. S. Casalongue, J. T. Robinson, Y. Y. Liang, Y. Cui and H. Dai, *J. Am. Chem. Soc.* 2010, **132**, 13978-13980.
- P. G. Bruce, B. Scrosati and J. M. Tarascon, *Angew. Chem., Int. Ed.* 2008, **47**, 2930-2946.
- Z. Li, X. Z. Zhan, D. Gao, Q. Xiao, G. Lei, *Electrochim. Acta* 2010, **55**, 4594-4598.
- H. Zhao, Z. Zheng, K. W. Wong, S. Wang, B. Huang and D. Li, *Electrochim. Commun.* 2007, **9**, 2606-2610.
- V. Palomares, P. Serras, I. Villaluenga, K. B. Hueso, J. Carretero-Gonzalez and T. Rojo, *Energy Environ. Sci.* 2012, **5**, 5884-5901.
- X. Su, Q. L. Wu, X. Zhan, J. Wu, S. Wei and Z. Guo, *J. Mater. Sci.* 2012, **47**, 2519-2534.
- H. Pan, Y. S. Hu and L. Chen, *Energy Environ. Sci.* 2013, **6**, 2338-2360.
- B. Li, H. Cao, J. Shao, G. Li, M. Qu and G. Yin, *Inorg. Chem.* 2011, **50**, 1628-1632.
- Y. Wang, X. Yu, S. Xu, J. Bai, R. Xiao, Y. S. Hu, H. Li, X. Q. Yang, L. Chen and X. Huang, *Nat. Commun.* 2013, **4**, 2365-2371.
- S. Maensiri, M. Sangmanee and A. Wiengmoon, *Nanoscale Res Lett.* 2009, **4**, 221-228.
- Q. Song, Y. Ding, Z. L. Wang, Z. J. Zhang, *Chem. Mater.* 2007, **19**, 4633-4638.
- L. Wang, X. Wang, J. Luo, B. N. Wanjala, C. Wang, N. A. Chernova, M. H. Engelhard, Y. Liu, I. T. Bae and C. J. Zhong, *J. Am. Chem. Soc.* 2010, **132**, 17686-17689.
- P. Hu, L. Yu, A. Zuo, C. Guo and F. Yuan, *J. Phys. Chem. C* 2009, **113**, 900-906.
- L. Tian, Q. Zhuang, J. Li, C. Wu, Y. Shi and S. Sun, *Electrochim. Acta* 2012, **65**, 153-158.
- S. Chen, Y. Wang, H. Ahn and G. Wang, *J. Power Sources* 2012, **216**, 22-27.
- L. Ji, M. Rao, H. Zheng, L. Zhang, Y. Li, W. Duan, J. Guo, E. Cairns and Y. Zhang, *J. Am. Chem. Soc.* 2011, **133**, 18522-18525.
- C. H. Lim, A. G. Kannan, H. W. Lee and D. K. Kim, *J. Mater. Chem. A* 2013, **1**, 6183-6190.
- Y. Zuo and Y. Wang, *ACS Nano* 2011, **5**, 8108-8114.
- Z. Jian, B. Zhao, P. Liu, F. Li, M. Zheng, M. Chen, Y. Shi and H. Zhou, *Chem. Commun.* 2014, **50**, 1215-1217.
- C. Zhu, X. Mu, P. A. van Aken, Y. Yu and J. Maier, *Angew. Chem. Int. Ed.* 2014, **53**, 2152-2156.
- P. Ramesh Kumar, Y. H. Jung, K. K. Bharathi, C. H. Lim and D. K. Kim, *Electrochim. Acta* 2014, **146**, 503-510.
- W. S. Hummers and R. E. Offeman, *J. Am. Chem. Soc.* 1958, **80**, 1339-1339.
- C. Santhosh, J. Ann Miriam, T. Malathy, M. Saranya, R. Ramachandran, S. Felix, T. Mudaliar Vanchinathan, V. Velmurugan and A. Nirmala Grace, *Nanosci. Nanotech-Asia* 2013, **3**, 120-126.
- J. Zhu, T. Zhu, X. Zhou, Y. Zhang, X. W. Lou, X. Chen, H. Zhang, H. H. Hng and Q. Yan, *Nanoscale* 2011, **3**, 1084-1089.
- Y. Shi, S. L. Chou, J. Z. Wang, H. J. Li, H. K. Liu, Y. P. Wu, *J. Power Sources* 2013, **244**, 684-689.
- P. Guo, G. Zhang, J. Yu, H. Li, and X. S. Zhao *Colloids Surf A Physicochem Eng Asp.* 2012, **395**, 168-174.
- N. N. Mallikarjuna, A. Lagashetty, A. Venkataraman, *J. therm. Anal. Calorim.* 2003, **74**, 819-826.
- Y. Feng, T. He, N. A. Vante, *ECS Trans.* 2008, **11**, 67-72.
- Y. J. Mai, D. Zhang, Y. Q. Qiao, C. D. Gu, X. L. Wang and J. P. Tu, *J. Power Sources* 2012, **216**, 201-207.
- X. Yinglin, Z. Jiantao, T. Liqi, L. Bo, H. Qianyan, Y. Chao and Q. Xuefeng, *Phys. Chem. Chem. Phys.* 2013, **15**, 3939-3945.
- P. Ramesh Kumar, Pratap Kollu, C. Santhosh, K. E. V. Rao, D. K. Kim and A. N. Grace, *New J. Chem.* 2014, **38**, 3654-3661.
- L. Su, Y. Zhong and Z. Zhou, *J. Mater. Chem. A* 2013, **1**, 15158-15166.
- Y. Shi, J. Z. Wang, S. L. Chou, D. Wexler, H. J. Li, K. Ozawa, H. K. Liu and Y. P. Wu, *Nano Lett.* 2013 **13**, 4715-4720.
- S. Bhuvaneswari, P. M. Pratheeksha, S. Anandan, D. Rangappa, R. Gopalan and T. N. Rao, *Phys. Chem. Chem. Phys.*, 2014, **16**, 5284-5294.
- P. Ramesh Kumar and Sagar Mitra, *RSC Adv.*, 2013, **3**, 25058-25064
- S. Mitra, P. S. Veluri, A. Chakraborty, R. K. Petla, *ChemElectroChem* 2014, **1**, 1068 - 1074.
- Y. Sharma, N. Sharma, G. V. Subba Rao and B. V. R. Chowdari, *Solid State Ionics* 2008, **179**, 587-597.